PROCEEDINGS, 41st Workshop on Geothermal Reservoir Engineering
Stanford University, Stanford, California, February 22-24, 2016
SGP-TR-209

Meso-Scale Field Testing of Reactive Tracers in a Model Geothermal Reservoir

Adam J. Hawkins[1,a], Don Fox[1], Matthew Becker[2] and Jefferson Tester[1,b]

[1]Cornell University, Cornell Energy Institute, Earth & Atmospheric Sciences and School of Chemical and Biomolecular Engineering, Ithaca, New York, 14850, USA

[2]California State University, Long Beach, Geology Department, 1250 Bellflower Boulevard, Long Beach, California, 90840, USA

[a]ajh338@cornell.edu

[b]jwt54@cornell.edu

Keywords: thermally reactive tracers, field studies, reservoir thermal hydraulics, modeling thermal breakthrough, fiber optic distributed temperature sensing, ground penetrating radar, flow channeling, short-circuiting

ABSTRACT

Meso-scale field testing of thermally reactive tracers was conducted at the Altona field site in a well-characterized, single sub-horizontal bedding plane fracture roughly 100 m^2 in active area located 8 meters below ground surface. The spatial distribution of subsurface groundwater flow was previously characterized using ground penetrating radar (GPR) measurements. The reservoir rock, initially at 11.7 °C, was heated using 74 °C hot water injection in a two-spot pattern using an injection to production well separation of 14 m. During the heating process, a series of thermally degrading tracer experiments were used to characterize the progressive *in situ* heating of the fracture. In addition, a conservative, carbon-cored engineered nanoparticle tracer was used to measure the residence time distribution (RTD) of fluid flowing from injector to producer. Fiber Optic Distributed Temperature Sensing (FODTS) was used to continuously measure the spatial distribution of heat exchange at ten locations spread out between the injection and production well. The experiments revealed reduced recovery of the thermally degrading tracer as the reservoir was progressively heated indicating that the advancement of the thermal front was proportional to the mass fraction recovered of the thermally degrading tracer. Both GPR imaging and FODTS measurements reveal that flow was reduced to a narrow channel which directly connected the two flowing wells and led to early and rapid thermal breakthrough. Computational modeling of conservative/reactive tracer and heat transport in a two-dimensional discrete fracture demonstrate that subsurface characterization using conservative tracers alone could not uniquely characterize the Altona field site. The inclusion of the thermally reactive tracer, however, provided improved resolution of the spatial distribution of flow after 1 day of hot water injection.

1. INTRODUCTION

Geothermal power plants commonly reinject production fluids in order to meet environmental and regulatory requirements to minimize water use, properly manage waste water, and prevent subsidence. In addition, reinjection may help maintain fluid production rates and prolong thermal extraction by potentially improving convection from hotter zones. Unfortunately, if short circuiting exists, reinjection will lead to production temperature decline as the rate of thermal energy extraction from the subsurface typically exceeds replenishment via natural thermal conduction and convective recharge. The onset and rate of temperature decline at the production well (i.e. thermal breakthrough) is a key consideration in determining the optimum fluid circulation rate because one must carefully consider the tradeoff between higher power production (via high fluid flow rate) and thermal breakthrough which reduces the thermodynamic quality (exergy) of produced fluid and lower power output per unit mass of fluid produced.

Predicting thermal breakthrough in reservoirs dominated by sparsely-spaced fractures is complex, due to uncertainties associated with the spatial distribution of fluid flow paths between injectors and producers. Unknown fracture geometry, particularly the distribution of fracture apertures, their lateral and radial extent, and the existence of fracture intersections contribute to this complexity. Even in individual horizontal fractures, flow can be highly heterogeneous and characterized by flow paths that do not follow a classic “dipole-flow” pattern in which fluid is spread out in a predictable manner between a single injection and production well (see Figure 1a). When heterogeneous flow results in fluid circulation concentrated through a smaller reservoir pore volume (i.e. flow channels) (Tsang and Neretnieks, 1998), the reduced volume of fluid circulation and surface area available for heat exchange may result in early and rapid thermal breakthrough which is referred to as “short-circuiting” (Figure 1c). “Premature thermal breakthrough” occurs when production temperature declines below power plant design specifications earlier than expected and could be economically disastrous for a commercial well field. In contrast, thermal breakthrough that occurs later and at a less rapid rate than a classic dipole-flow would indicate that the permeability directly between an injection well and production well is less than the areas of the fracture outside this region (Figure 1b). In such a case, an increased mass flow rate may be advisable permitting greater energy production. A drawback, however, may be low injectivity/productivity and loss of injected fluid.

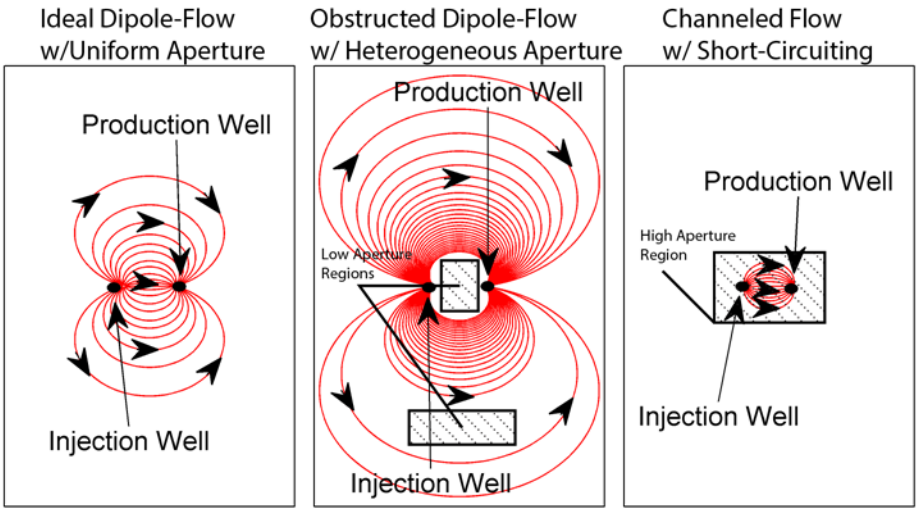

Figure 1: Streamlines (red) and velocity direction (black arrows) induced via a two-spot well pattern in a single discrete fracture with a.) ideal dipole-flow with uniform aperture fracture, b.) obstructed dipole-flow with variable aperture distribution, and c.) channeled flow with inlet/outlet well short-circuiting. The dipole-flow pattern in figure "a" results from flow induced in a uniform aperture fracture. A heterogeneous fracture aperture field can result in greater heat transfer surface area (figure a) if a region of low aperture persists directly between two wells. In contrast, a region of high aperture directly between two wells can lead to flow short-circuiting (figure c), which would reduce thermal performance.

Due to the uncertainties involved in predicting thermal breakthrough, techniques to actively monitor a cold thermal front as it migrates from injection to production wells are desired. Thermally reactive chemical tracers, which are sensitive to subsurface changes in temperature distribution, were proposed nearly 30 years ago as a viable means to monitor transient subsurface temperature (Robinson et al., 1988). Thermally reactive tracers are selected based on temperature-dependent reaction properties over the range of *in situ* reservoir temperatures anticipated between wells. Residence Time Distributions (RTDs) of both inert and reacting tracers are used to estimate the degree of thermal drawdown by contrasting an initial tracer experiment conducted in an initially hot reservoir with the results of a second experiment in which some reservoir cooldown near the injection well has occurred. In the second experiment, less reaction progressed, because the tracer encountered reduced temperatures for a portion of its residence time in the subsurface. In principle, the tracer mass fraction reacted is proportional to the extent of reservoir cooling. Conducting a series of thermally reactive tracer tests could map the progression of the cold thermal front as it approaches a production well prior to observing thermal breakthrough at the production well. This knowledge could permit more accurate optimization of production rates which may improve reservoir lifetime and/or increase power production.

While thermally reactive tracers have long been considered a viable means to characterize subsurface reservoir temperature distributions, they have been rarely used in actual field experiments and, to the best of our knowledge, have never been successfully validated. The objective of this study was to demonstrate, in the field, that a thermally reactive tracer can provide an indication of a thermal front's progression from injection well to production well. Full-scale geothermal reservoirs operate on spatial and temporal scales that require operating times on the order of months to years to produce measureable thermal breakthrough at production wells. As a result, conducting field experiments in a full-scale reservoir is unrealistic given the time constraints and the experimental controls required in this study. By conducting field experiments at a meso-scale these constraints were alleviated. For example, thermal breakthrough is achievable within days using a reservoir constrained by a short injection to production well separation distance of order 20 m or less.

2. GOALS AND APPROACH

Conservative tracers are invaluable in providing quantitative information regarding RTD and overall reservoir volumes. However, they are inadequate for describing the progress of cooling within a geothermal reservoir undergoing heat extraction. As a result, this study focused on utilizing laboratory-tested thermally reactive chemical tracers in field tests at the Altona, New York site in order to demonstrate their feasibility in a well-defined meso-scale fracture system (Becker et all., 2013; Becker and Tsoflias, 2010; Guiltinan and Becker, 2010; Hawkins and Becker, 2012; Hawkins et al., 2015; Tsoflias et al., 2012; Tsoflias et al., 2015).

Based on heuristics verified by earlier computational modeling in our group (Fox et al., 2015) we have shown that fracture aperture distribution has a strong influence on the available heat transfer surface area and will ultimately control thermal breakthrough. A major goal of this study is to evaluate how effective thermally reacting tracers are in providing more accurate determinations of fracture aperture characteristics that control flow channeling and have a substantial influence on thermal

breakthrough. In addition, predictions from computational models of tracer/thermal breakthrough will be compared to experimentally observed data to better understand how fracture volumes, mean apertures and aperture distributions influence thermal performance.

The specific approach of this study was to:

1. Select appropriate conservative and thermally reactive tracers for use at the Altona site.
2. Measure tracer RTD and thermal breakthrough under steady-state injection/production flow conditions using both conservative and thermally reactive tracers.
3. Record the spatial distribution of temperature change within the fracture and the surrounding rock matrix in-between the injection and production well.
4. Use computational models and observed field data to characterize the flow and fracture aperture distributions consistent with the experimentally observed tracer/thermal breakthrough.

3. METHODS

3.1 Field Site

The field site is located in the Altona Flat Rocks, in northern New York, USA about 6 km northwest of West Chazy, New York. The Altona Flat Rocks region is unique in the Northeastern United States, because a glacial flood stripped soil overburden off of bedrock, exposing an expanse of sandstone with shallow groundwater in bedrock fractures (Rayburn et al., 2005). The relevant formation, the Cambrian-aged Potsdam Sandstone, is well cemented with silica and as a consequence has a matrix (or "primary") porosity of roughly 1 percent. Ubiquitous fracturing, however, makes the formation highly permeable and it is commonly used as an aquifer for drinking water supply (Olcott, 1995).

The Altona Flat Rocks locale where the experiments were conducted is located in the William H. Miner Experimental Forest (http://www.whminer.com/). The experimental site was selected due to its lack of soil cover, the shallow water levels, and the presence of strong sub-horizontal bedding plane fracturing. Reconnaissance Ground Penetrating Radar (GPR) surveys located a reflection at 7.6 m deep that was interpreted to be an open bedding plane fracture. Subsequent drilling of a well field in 2004 confirmed the location of a permeable fracture that was suitable for conducting tracer and hydraulic testing. Since the drilling of the wells, multiple experiments have been carried out at the site to investigate flow and solute transport (Becker and Tsoflias, 2010; Castagna et al., 2011; Guiltinan and Becker, 2010; Hawkins et al., 2015; Talley, 2005; Talley et al., 2005; Tsoflias and Becker, 2008; Tsoflias et al., 2015).

The well field is located near an abandoned dam (Skeleton Dam) which creates a strong hydraulic gradient of roughly 0.004 [-] across the well field as water flows from the artificial reservoir (Chasm Lake) to a small ledge which produces a seepage face (see Figure 2) (Becker and Tsoflias, 2010). A five-spot 15 cm diameter well pattern penetrates a conductive sub-horizontal fracture 7.6 m below the surface. Transmissivity of the fracture is estimated to be about 5 m^2/day which suggests a mean hydraulic aperture of about 0.5 mm based upon the local cubic law (Talley et al., 2005). Two groundwater tracer experiments conducted between wells 404 and 304 as well as between wells 404 and 104 suggest a mean fracture aperture between 0.8 and 1.0 mm (Hawkins et al., 2015). For all experiments, the target bedding plane fracture was isolated with inflatable packers in order to isolate a single sub-horizontal flow field.

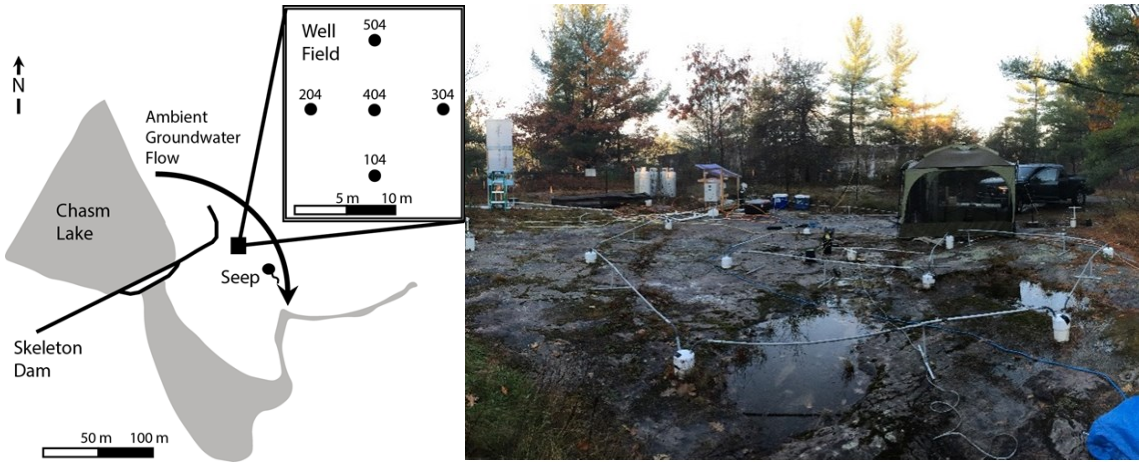

Figure 2: Map of the Altona field area and well field (left) and a photograph of the wellfield taken in October 2016 (right).

The wells of the five-spot configuration, drilled using a water rotary drill in May of 2004, are 15 cm in diameter and were originally drilled to a depth of 12.2 m with a 0.91 m surface casing and open borehole below. In July of 2011, all five wells were

deepened with percussion air rotary drill with a 14 cm diameter bit. The new well depths ranged from 18.3 m to 21.3 m. PVC casings were installed from ground surface to roughly 0.7 m below ground surface. An open borehole in the sandstone rock remained below the bottom of casing. Roughly 15 to 30 cm of PVC casing was left exposed above ground surface. Bentonite clay was used to seal the casing to the formation.

The ten dry boreholes in which the fiber optic cable was installed were also drilled in July of 2011. These ten boreholes were drilled to 7 m below ground surface, or about 60 cm above the fracture investigated in this study. To prevent surface runoff into the boreholes, a 15 cm diameter well casing was installed in the top meter with an additional 20 to 45 cm exposed at the surface.

3.2 Fiber Optic Distributed Temperature Sensing (FODTS)

DTS is a relatively new means of thermometry (developed in the 1980s) that has high temporal and thermal resolution. Temperature measurements are made along a fiber-optic cable by observing the backscatter of laser light projected along the fiber (Smolen and Spek, 2003). An Oryx DTS (Sensornet Ltd) was rented from the Center for Transformative Environmental Monitoring Programs (CTEMPs) which is funded by the National Science Foundation and jointly operated by Oregon State University, Corvallis and the University of Nevada, Reno. The Oryx collects temperature measurements on a sampling interval of 1 m. In laboratory experiments conducted by Adam Hawkins at California State University, Long Beach in 2010, the spatial resolution was found to be 2.4 m. In this context, spatial resolution is defined as the distance along the fiber optic cable required for the Oryx DTS to respond to 80% of a step change in temperature. See Smolen and Spek (2003) for further details on how spatial resolution is determined. Sensornet's Oryx DTS data sheet states an optimum temperature resolution of ±0.01 °C when collecting laser backscatter data continuously for 30 mins (Sensornet, 2007). This resolution worsens continuously with increasing distance traveled along the fiber optic cable. At 1500 m, the spatial resolution is ±0.02 °C when collecting data for 30 mins.

For our purposes, the DTS spatial sampling interval in the boreholes had to be improved because of the short distance from the fracture over which heat flow was measured. The sampling interval was improved from 1 m to 2.1 cm by wrapping the fiber optics around a specially fabricated, externally threaded, 5.7 cm, schedule-80 PVC pipe. Fiber optics were wrapped around the threaded pipe using modified lathe and spool feed. Two coils of cable were left at the top of each pipe enable to arc fusion splice the fiber optics of each borehole in the field. The wrapped pipes were then shipped to New York where they were placed within each borehole and arc fusion spliced using a Fujikura SpliceMate™ in the summer of 2011. Five pipes were 3 m in length and five were 1.5 m.

The process of wrapping fiber-optic cable around a threaded PVC pipe increases the attenuation of light within the fiber optic cable, therefore decreasing the maximum length of cable suitable for accurate DTS deployment. To reduce the impact of bending, a high numerical aperture fiber optic cable (AFL, model DNS-2528) with a 41 mm static bend radius was used.

The 8.3 cm open annulus between the fiber optic cable and the borehole wall was filled with a mixture of sand and water in order to create sufficient thermal coupling between the rock formation and the fiber optic cable. Clean sand (Quickrete © Play Sand #1113) was introduced into the borehole roughly 0.5 L at a time and water was poured in-between to wash sand from the sides of the borehole. The wrapped cable rod was vibrated during pouring to assure compaction.

DTS calibration was performed utilizing a "two-way" (or double ended) approach in which the fiber optic cable was connected to the DTS at both ends of the cable (van de Giesen et al., 2012). This required two channels on the DTS which independently pulse light through the fiber optic cable. Two-way measurements allow for correction in temperature measurements due to local signal loss and transmission attenuation as light travels within the fiber optic cable.

An inherent systematic drift in the baseline related to the internal temperature of the DTS unit (in the range of 1 to 2 °C for each DTS temperature measurement) was present in the FODTS system. This drift was corrected for using two temperature control baths at ground surface which both contained roughly 50 m of fiber optic cable. One bath was filled with an ice/water mixture which was kept at roughly 0°C for the entire duration of the experiment. The other bath contained groundwater pumped from the site and the water temperature was allowed to fluctuate naturally with the ambient atmospheric temperature. Temperature transducers (RBR solo®) recorded temperature in each bath every 2 minutes for the entire duration of the experiments and an aquarium air pump mixed the water in each bath to prevent temperature gradients from forming. The transducer temperature measurements were used to correct the FODTS temperature measurements.

Sometime between the installation of the fiber optic network in early August 2011 and the return trip in late October 2011 the network was inadvertently damaged by natural forces or unauthorized site visitors. Two segments of the network (b10 and b7 in Figure 6) were damaged and one segment, b9, had to be installed with the bottom of the threaded pipe at 1.5 m above the target fracture rather than the desired 0.6 m. In June of 2015 the damaged segments of the fiber optic network in the two boreholes were repaired.

3.3 Heat Exchange Experiment

The heat exchange experiment was conducted under forced convection conditions between an injection and production well. Prior to reinjection into the formation the water was heated with a propane-fired tankless water heater (AO Smith, Model #: T-

H3-OS) up to 74 °C. Flow was induced by a variable speed positive displacement pump (Rediflow-2, Grundfos). Production water was directly reinjected into the injection well after circulating through the tankless water heater. Flow rate was maintained at 6 L/min and was monitored using the digital flow gauge accompanying the tankless water heater. Manual flow measurements confirmed the accuracy of the digital readout. Injection and pumping were conducted from a hydraulically isolated zone in the wellbores that were aligned with the 7.6 m deep test fracture. Hydraulic isolation in the injection well, pumping well, and three observation wells was achieved using two modified inflatable pipe packers (Lansas Products, Lodi, California) in each well and the spacing in-between the two packers ranged from 0.2 to 0.5 m.

Water temperature and hydraulic head in three monitoring wells (wells 104, 404, and 504) was recorded via autonomous pressure/temperature loggers (Solinst Leveloggers®, Model #: 3001). Each logger recorded temperature (0.003 °C resolution) and head (resolution of 0.0006 to 0.002% of the maximum depth) every 2 mins throughout the experiment. To account for variations in barometric pressure, a reference pressure transducer (Solinst Barologger®, model #: 3001) was placed on the ground surface. A temperature transducer (RBR solo®) was placed within well 304 to monitor production well temperature.

Circulation between the injection well and production well began 5.8 hrs prior to hot water injection. Hydraulic head measurements in observation wells 104, 404, and 304 all recorded steady state hydraulic head 2 hrs prior to the onset of hot water injection. Over the course of the 2 hrs prior to hot water injection 62 water temperature measurements in the production well recorded an average temperature of 11.74 °C with a maximum and minimum of 11.72 °C and 11.76 °C, respectively. Once steady-state water levels were achieved in the monitoring wells, the experiment was initiated by turning the tankless water heater on. Injection temperature was monitored at the outlet of the heater using the thermometer accompanying the tankless water heater. Injection temperature remained at 74 ± 2 °C for the duration of the experiments.

3.4 Tracer Testing

A nanoparticle tracer, referred to as "C-dots", was used as a conservative tracer. The C-dot nanoparticle tracer consists of a carbon core decorated with a highly fluorescent polymer. The particles are synthesized in a one-step process from citric acid and ethanolamine (Krysmann et al., 2012). The 3-5 nm diameter particles are highly water soluble and inert (Li et al., 2014). They have a very low molecular diffusivity, and are detectable by their fluorescence to concentrations of ~1 ppb in deionized water. Similar carbon-cored particles have been developed for medical applications where they have been demonstrated to have very low toxicity (Ray et al., 2009). Previous field experiments at the Altona field site in June of 2014 demonstrated that the C-Dots behave as conservative tracers as evident by comparisons between the RTD of an anionic iodide tracer and the C-Dot tracer (Hawkins et al., 2015) Although this particular nanoparticle tracer was ideal for Altona, it is currently unstable at temperatures greater than that at which they were synthesized (200 °C). Active research is underway to synthesize similar particles at higher temperatures in order to permit their use at temperatures above 200 °C, which are frequently encountered in commercial hydrothermal reservoirs.

Phenyl acetate was used as the thermally reactive tracer as it undergoes a rapid temperature-dependent hydrolysis reaction. Phenyl acetate reacts in the presence of water to form phenol and acetate and is dependent on fluid pH and temperature (Figure 3). Since pH was found to be constant during the entire heat exchange experiment (pH=6.52), the reaction rate was dependent only upon the fluid temperature in the subsurface. This reaction follows a (pseudo-) first order reaction with a reaction rate constant, k, dependent upon temperature as described by the Arrhenius law:

$$k = A \cdot exp\left(-E_a/(RT)\right) \tag{1}$$

where A is the pre-exponential factor [hr^{-1}], E_a is the activation energy [kJ/mol], R is the universal gas constant [kJ/mol-K], and T is the absolute temperature [K]. A detailed description of the use of phenyl acetate as a reactive geothermal tracer is described in Nottebohm et al. (2012) and laboratory experimental validation is described in Maier et al. (2015).

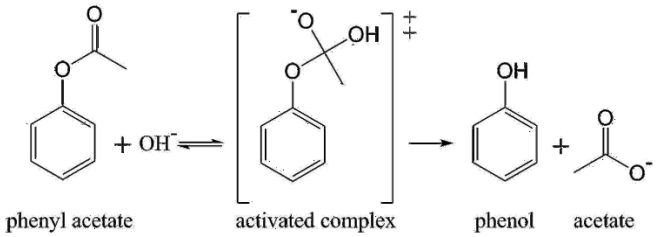

Figure 3: Base-catalyzed hydrolysis of phenyl acetate to produce phenol and acetate (Nottebohm et al., 2012). Phenyl acetate was used as a thermally degrading tracer in the field experiments conducted at the Altona Site.

Within 1 min of sample collection, both C-Dots and phenol were analyzed using a fluorescence spectrometer from Varian (Model #: G9800A). The peak excitation/emission wavelength for C-Dots and phenol in Altona groundwater was found to be 358/440 nm and 267/297 nm, respectively. The detection limit for C-dots and phenol in Altona ground water was found to be roughly 50

ppb. Groundwater samples were collected using a PVC ball valve to sample fluid at the ground surface in 30 mL Nalgene bottles. Samples were taken from the well field to the spectrometer located in a wooden shed roughly 30 m from the well field. Air temperature in the shed was monitored throughout the tracer experiments.

Because of the high reaction rates associated with phenyl acetate hydrolysis at temperatures encountered in these field experiments (roughly 10 to 75 °C), analysis of each groundwater sample was completed within 1 min of collection to prevent significant reaction after collection. Fluorescence of the phenol product was determined to be the most effective detection method, because samples can be rapidly analyzed without the need for sample preparation. The use of a Gas Chromatograph with a Flame Ionization Detector (GC-FID) after separation via Solid Phase MicroExtraction (SPME) could be used to detect both phenyl acetate and phenol. However, sample analysis via GC-FID was found to require, at minimum, 30 mins per sample in analysis trials conducted by Adam Hawkins at Cornell University and may take longer depending on the GC method and desired detection limit. Due to the short duration of the tracer experiments (< 3 hrs), the high reaction rates, and the complexities involved in deploying GC-FID in the field, GC-FID was not considered a practical analytical method for these field experiments.

As in the heat exchange experiment, conservative/reactive tracer experiments were conducted under forced convection conditions between an injection and production well. The first tracer test was conducted 1 day prior to hot water injection. The remaining two tracer tests were conducted during the heat exchange phase of the field experiment. As described in Section 3.3, a variable speed positive displacement pump (Rediflo-2, Grundfos) was used to establish a steady-state flow field. To introduce the tracer solution, an approximately 2 L solution consisting of 250 ppm phenyl acetate and 100 ppm C-dots was placed in a bypass PVC pipe directly inline between the injection and production well prior to entering the tankless water heater. When the tracer was ready to be injected, two valves were opened to allow flow through the bypass pipe. The bypass pipe minimized disturbance to the subsurface hydraulic gradient field that may have resulted from other means of introducing tracer, such as gravity drainage of the tracer solution through a funnel into the top of the injection well.

3.5 Computational Reservoir Modeling

Computational modeling of fluid, heat, and tracer transport in a discrete fracture with heterogeneous permeability was accomplished using a finite element method (FEM) solver developed by our group (Fox et al., 2015). The model was used to simulate the effects of varying aperture distributions on the spatial distribution of heat exchange, thermal breakthrough, and conservative/reactive tracer RTD. This numerical model is a hybrid finite element and boundary element method for discretely fractured geothermal reservoirs. Three-dimensional heat conduction in the rock matrix is captured through a boundary element treatment while fluid flow is solved via the FEM. The rock matrix surrounding the discrete fractures is assumed to be impermeable with respect to fluid flow.

Fluid advection was modeled as a flow of a Newtonian fluid in a thin fracture that is mathematically represented as a rectangular channel with a specified aperture. An internal fluid pressure field within the fracture was induced by an injection well (source) and production well (sink) under steady-state flow conditions. There is a no-flux boundary condition at the surfaces of the fracture and the edges of the fracture domain. Combining a reduced Navier-Stokes equation and the solution for Poiseuille flow (as described in Fox et al. (2015)), the pressure field can be determined from the following equation:

$$-\nabla\cdot\left(\frac{\rho_w w^3}{12\mu}\left[\nabla P-\rho_w\mathbf{g}\right]\right)=\sum_l \dot{m}_l\delta\left(\mathbf{r}-\mathbf{r}_l\right) \tag{2}$$

where ρ_w, w, μ, P, ρ_w, and $\mathbf{g}$ are fluid density, fracture aperture, dynamic fluid viscosity, pressure, and gravitational acceleration, respectively. The right hand side of the equation describes the influence of sources and sinks where $\dot{m}$ is the mass flow rate of each source or sink, $\delta(...)$ is the Dirac delta function, and $\mathbf{r}$ is the position in the fracture. The symbol $\mathbf{r_l}$ represents the position of the sources and sinks in the fracture plane. The two dimensional pressure gradient is on the plane of the fracture. Once the pressure field is determined via the FEM using Equation 2, the average velocity across the fracture aperture, $\mathbf{v}$, was calculated by

$$\langle\mathbf{v}\rangle=-\frac{w^2}{12\mu}\nabla P\,. \tag{3}$$

Assuming negligible transient heat accumulation in the liquid contained by the fracture and negligible thermal conduction through that liquid, the fluid energy balance inside the fracture is given by

$$q_s=\rho_w c_w w\langle\mathbf{v}\rangle\cdot\nabla T \tag{4}$$

where q_s is the surface heat flux from the fracture surface going into the fluid and c_w and T are the heat capacity of water and temperature, respectively. The two dimensional temperature gradient is on the plane of the fracture. Because the surface heat flux depends on the rock conductivity and temperature gradient orthogonal to the fracture surface, Equation 4 cannot be solved independently. A three-dimensional Green's function was used to present the temperature of the system dependent on the fracture

surface heat flux, as described in Fox et al. (2015). The governing equation for thermal conduction in the rock matrix surrounding the fracture is

$$\rho_r c_r \frac{dT}{dt} - \nabla \cdot (k_r \cdot \nabla T) = q_s \delta(z - z') \tag{5}$$

where ρ_r, c_r, k_r, and z are the density, heat capacity, thermal conductivity, and distance orthogonal to the fracture. The subscript r refers to the rock material, z' refers to the position, orthogonal to the fracture, of the heat source, q_s, and $\delta(...)$ is the Dirac delta function. For Equation 5, the spatial dimension of the temperature gradient, ∇T, is three dimensional. For a heat source located at $z=0$ and confined to the extent of the fracture, the temperature of the system is expressed as

$$T(x, y, z, t) = T_r + \int_0^t \int_A G(x - x', y - y', z, t - t') \frac{q_s(x', y', t')}{\rho_r c_r} dx' dy' dt' \tag{6}$$

where G and T_r are the 3D Green's function for transient conduction and the original reservoir rock temperature, respectively.

As was done in the heat transport model, the pressure field within the fracture for the tracer test simulations was solved via the FEM. In addition, tracer advection, dispersion, and thermal degradation were also solved via the FEM. The tracer mass balance inside the fracture includes transient accumulation of tracer, tracer dispersion, advective bulk flow, and chemical reaction and can be represented in the following governing equation:

$$w\frac{\partial c}{\partial t} = wD_f \nabla^2 \mathrm{c} - \mathrm{w}\langle \mathbf{v} \rangle \cdot \nabla \mathrm{c} - \mathrm{w}k\mathrm{c} \tag{7}$$

where c, t, D_f, $\langle v \rangle$, and k are tracer concentration, time, dispersion coefficient, velocity, and reaction rate constant, respectively. The reaction rate constant, k, follows a first-order reaction rate with an Arrhenius temperature dependency (Equation 1). The spatial dimension of the concentration gradient ∇c is in the two-dimensional plane of the fracture. Rather than using the computationally intensive Laplace domain in which heat transport was solved, time discretization was performed via the Crank-Nicholson method. The dispersion coefficient, D_f, is a function of fluid velocity, hydrodynamic dispersivity, α, and chemical diffusion, D^*, and is expressed as

$$D_f = \alpha \langle \mathbf{v} \rangle + D^* . \tag{8}$$

When simulating temperature-dependent chemical reactions, first the temperature field after a specified time of circulation is solved followed by the tracer concentration field. Since the timescale of tracer residence time is typically on a scale much less than energy extraction/injection, it is appropriate to assume the temperature of the subsurface does not change during the timespan of a tracer test. Thus, one does not need to solve a coupled equation for heat and tracer transport in order to solve for the concentration field.

Thermal conductivity of the Potsdam Sandstone at the Altona site was measured using the RK-1 Rock Sensor Package of the KD2 Pro manufactured by Decagon Devices. A value of 7.6 W/m-K was recorded in a rock sample collected from ground surface at the well field. The measured thermal conductivity is slightly greater than the maximum value for sandstone published in Robertson (1988) which ranges from 5 W/m-K to 7.5 W/m-K for sandstones with 60-90% quartz, 0-10% matrix porosity, and water filled pores. Density of the Potsdam Sandstone was determined to be 2.5 g/cm^3 by weighing a rock sample collected at ground surface and measuring its volumetric displacement in water. Specific heat was assumed to be 930 J/kg-K based on reported average values of sandstone in Robertson (1988). Specific heat and density of water was assumed to be 4200 J/kg-K and 1 g/cm^3, respectively, appropriate for the temperature conditions at Altona.

3.6 Ground Penetrating Radar (GPR) Measurements for Reservoir Characterization

Surface-based reflection GPR has been used at this field site to image fracture fluids at the Altona field site. Two kinds of measurements were used; a "background" survey in which natural water is in place and a "saline" survey in which a relatively constant concentration of saline solution is continuously circulated between an injection and production well. GPR imaging without saline solution provides a relative measure of the spatial distribution of fracture aperture, because a larger water-filled aperture leads to a greater reflection amplitude and phase measured at ground surface. Subtracting the background survey from the saline survey produces an image of the spatial distribution of NaCl in the fracture and thus provides maps of the spatial distribution of groundwater flow paths between an injection and production well.

These surveys preceded the thermally reactive tracer measurements in this study and are reported in detail by Becker and Tsoflias (2010) and Tsoflias (2015). In these tracer imaging experiments, saline water was injected in well 304 and pumped from well 204. The distribution and transport of salt water in the fracture was determined by measuring the electromagnetic phase change

between the incident and reflected EM waveform (Tsoflias and Becker, 2008). Phase measurements in pairs of 100 MHz antennae oriented orthogonal to one another were summed, to remove the effect of polarization from the reflected signal (Tsoflias et al., 2015). In the imaging mode of interest here, saline water is continuously circulated between well pairs while radar antennae are moved about the surface. The grid of these measurements, with spacing of 0.25 m along lines separated by 0.5 m intervals, was contoured to produce maps of phase response in the fracture which are approximately linearly related to fluid salinity.

GPR imaging of natural water present within the fracture reveals a spatially correlated and anisotropic distribution of fracture aperture (Figure 4 - left). The spatial distribution of fracture aperture is represented by the strength of the amplitude, measured in relative amplitude units. Therefore, the areas of largest fracture aperture exist where the greatest amplitudes were measured. The figure reveals a narrow region of large aperture which persists in a direction oblique to the direct path between wells 204 and 304 at an angle of 25°. The channel is roughly 2 to 4 m in width and appears to extend beyond the surveyed area. The background survey therefore reveals potential for flow channeling between wells 204 and 304.

GPR imaging of saline water circulated between well 304 and 204 reveals a strong, direct flow path directly between the injection and production well (Figure 4) over a distance of 14 m. The spatial distribution and concentration of saline tracer is represented by the strength of the phase shift, measured in degrees, between the phase measured prior to and during tracer circulation. Therefore, the areas of greatest tracer concentration existed where the greatest phase shift was measured. The width of the flow channel directly connecting the two wells is approximately 4 m. The strongest phase shift, roughly -90 to -80 degrees, occurred in a narrow, roughly 1 m wide path conducted dominantly in a direct path between the two wells. The region around observation well 104 had very little to no change in phase during this survey suggesting that injected fluids did not flow through this region. Similarly, although to a lesser extent, the region around observation well 504 experienced very little change in phase.

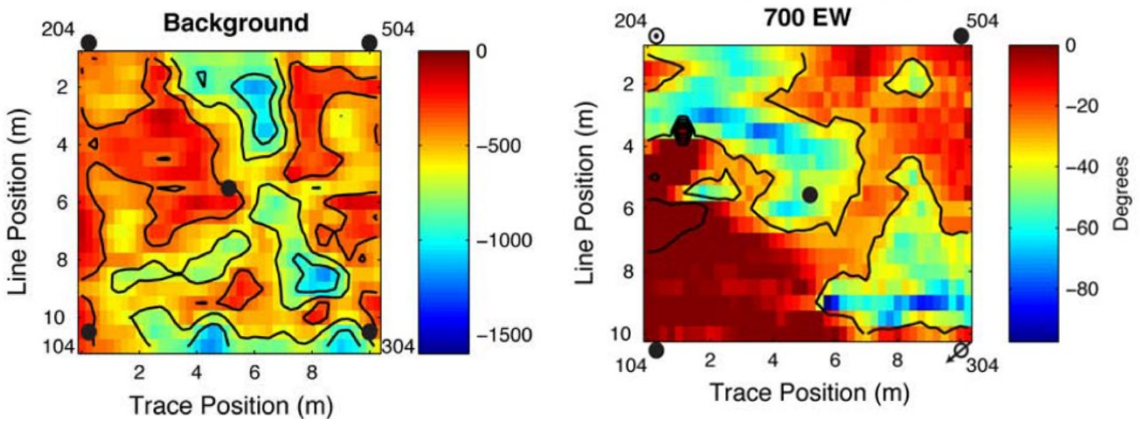

Figure 4: Map of the background survey (left) and the saline survey (right). The background figure provides a relative measure of the fracture aperture distribution throughout the site where a greater amplitude (blue colors on the figure) represent larger fracture aperture. Phase offset, as shown in the figure to the right, is approximately linearly related to fluid salinity. Yellow and blue colors in the figure to the right, therefore, indicate the presence and concentration of saline fluid circulated between wells 304 and 204. Note that the injection well in the GPR study was well 304 and the production well was well 204 (the opposite flow direction as the heat exchange experiment and the tracer tests presented in this paper).

4. RESULTS

4.1 Reservoir Heat Exchange Experiment

The heat exchange experiment lasted 140 hours at a fluid circulation rate of 6 L/min with a total volume circulated of 50,400. FODTS began detecting temperature rise 83 mins after hot water injection began at borehole b8. By the end of the experiment, temperature rise was recorded in all boreholes. The greatest temperature rise among the boreholes occurred at the deepest measurement point and ranged from 0.9 °C in borehole b2 to 22.9 °C in borehole b8 (Figure 5). The boreholes which experienced the greatest temperature rise were spatially distributed in a narrow path directly between the injection well and production well (Figure 6).

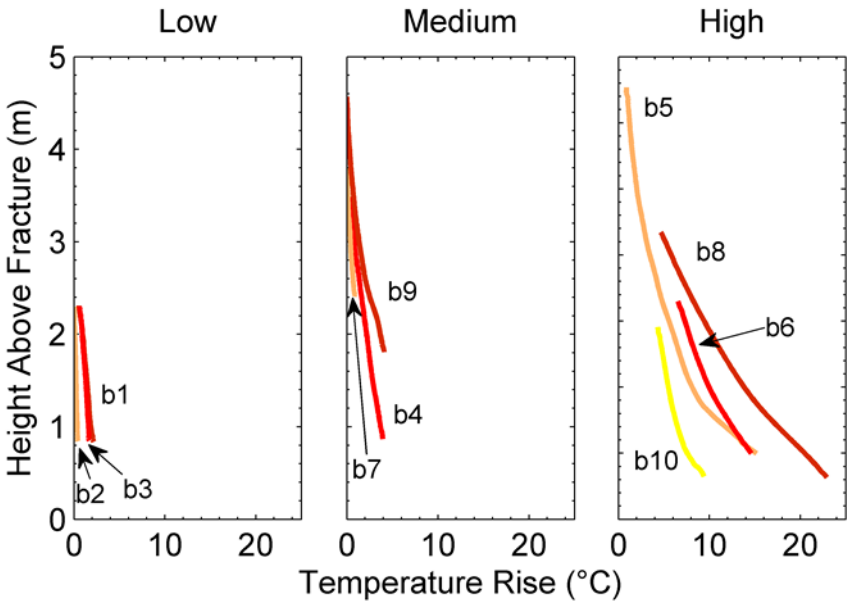

Figure 5: Temperature rise vs. height above the fracture surface for all 10 monitoring locations after 140 hrs of hot water circulation. The graphs are separated by the relative magnitude of temperature rise with the designations low, medium, and high. These designations are the basis for the qualitative map view representation of temperature rise shown in Figure 6.

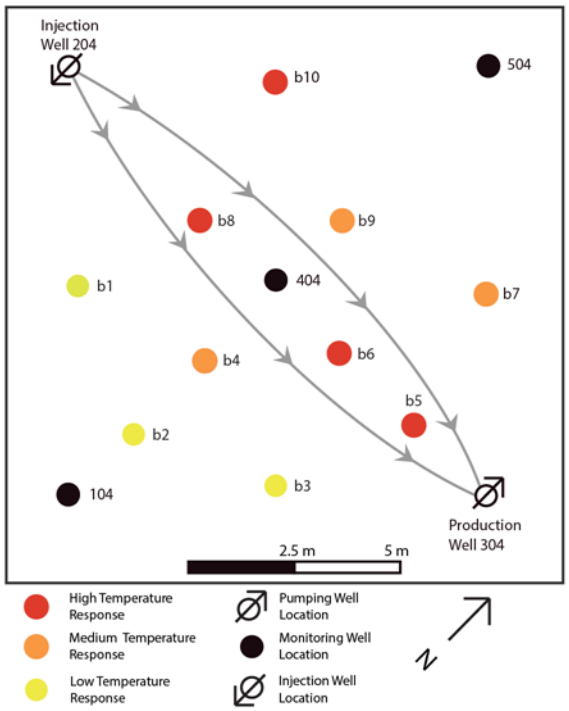

Figure 6: Qualitative map view representation of temperature rise, as recorded via FODTS. Heat exchange is generally greatest in a narrow path directly between the injection and production well. The colors of the temperature response points are based on data presented in Figure 5. The grey arrows represent the general direction of fluid transport in the fracture from the injection well to the production well.

At the production well, groundwater temperature was stable at 11.7 °C until the onset of thermal breakthrough 48 mins after the initiation of hot water injection. Thermal breakthrough roughly followed a power law time dependence. From 1.3 hrs to 4 hrs into

the heat exchange experiment, the maximum slope of production temperature was 0.7 °C/hr. The slope fell to 0.04 °C/hr by the end of the experiment after 140 hrs of hot water injection (Figure 7). Reservoir fluid temperature at the production well rose 17.4 °C from 11.7 °C to 29.1 °C which corresponds to 28% of the difference between the initial temperature of groundwater pumped at well 304 and the temperature of water reinjected into well 204 (74 °C).

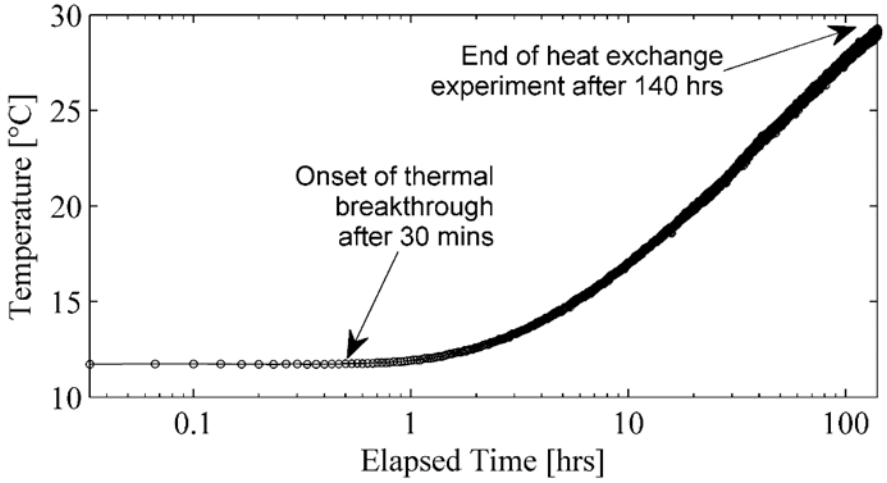

Figure 7: Measured production well temperature as a logarithmic function of time for the entire 140 hr experiment. The onset of thermal breakthrough at the production well occurred after 30 mins of hot water injection which corresponds to a measureable rise of 0.03 °C in the production fluid followed by a relatively continuous increase in temperature for the remainder of the experiment.

4.2 Tracer Experiments

A tracer test was conducted 1 day prior to heat injection. Two additional tracer tests were conducted while the reservoir was being heated; the first was conducted after 1 day of hot water injection and the second after 3 days. In each experiment both C-Dots and phenyl acetate were used as tracers. The RTD of the C-Dot tracer was nearly identical in each of the three tracer tests. The thermally reactive tracer phenyl acetate showed reduced concentration in each of the three tests (Figure 8). The initial thermally reactive tracer test, conducted 1 day prior to the onset of hot water injection, experienced significant reduction in phenyl acetate concentration.

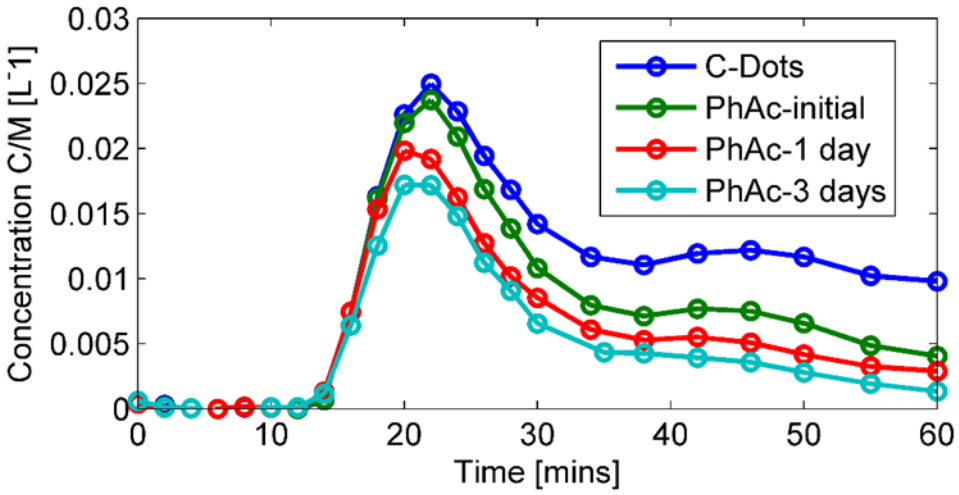

Figure 8: RTDs for the three phenyl acetate reactive tracer tests and the average of the C-Dot RTDs. "Initial" refers to the reactive tracer RTD prior to hot water injection. "1 day" and "3 days" represent reactive tracer RTD after 1 and 3 days of hot water injection, respectively. Because the mass of C-Dots injected was different than phenyl acetate, concentration is normalized to initial tracer mass injected. Concentration, C, is normalized to the initial tracer mass injected, M, and is calculated by C/M. The second peak in each of the curves (at approximately 42 mins) resulted from reinjection of produced fluids back into the injection well.

4.3 Computational Reservoir Modeling

Two scenarios representing end-member cases were considered in the modeling effort. The first involved a discrete fracture of constant aperture (subsequently referred to as the "ideal dipole-flow scenario") while the second considered the effect of a narrow region of large aperture directly in-between the injection and production well (subsequently referred to as the "channeled-flow scenario". Neither scenario is represents the true fracture aperture distribution, but simulating tracer and heat transport using the two end-member cases allows one to identify which case is more realistic.

Several steps were involved in the computational reservoir modeling effort. First, agreement between the experimentally observed and simulated conservative tracer curves was made by manually varying the fracture aperture and hydrodynamic dispersivity (Figure 10). The observed C-Dot RTD was fit well by both scenarios. Best-fit parameters in the ideal dipole-flow scenario consisted of a fracture aperture of 0.7 mm with a dispersivity of 8 cm. The channeled-flow scenario consisted of a 1 m wide region directly connecting the injection and production well with a fracture aperture of 5.7 mm and a surrounding region with an aperture of 1.9 mm; dispersivity in this case was 20 cm (see Figure 9 for a map view of the fracture aperture distribution for both scenarios).

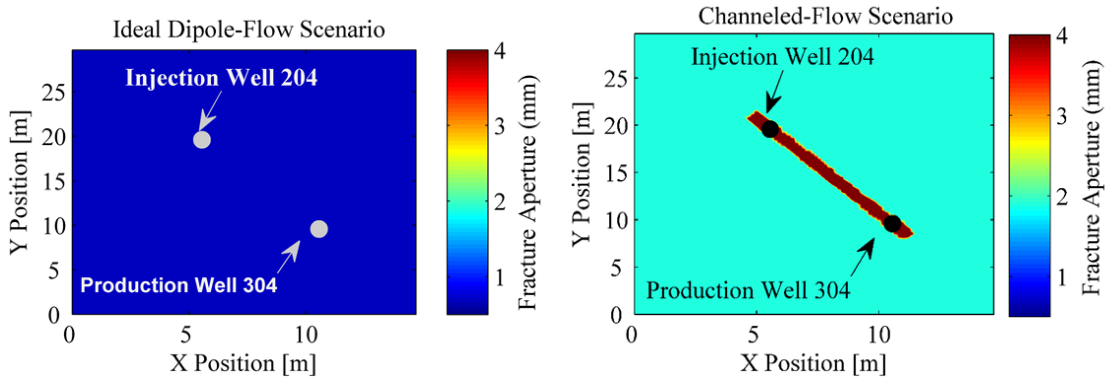

Figure 9: Map view of fracture aperture spatial distribution used in discrete fracture FEM simulations for the "ideal dipole-flow scenario" (left) and the "channeled-flow scenario" (right). Results of the conservative tracer simulations for both scenarios are presented in Figure 10. The "ideal dipole-flow scenario" has an aperture of 0.7 mm whereas the "channeled-flow scenario" has a 1 m wide region of 5.7 mm fracture aperture directly between the two wells surrounded by a uniform aperture region of 1.9 mm.

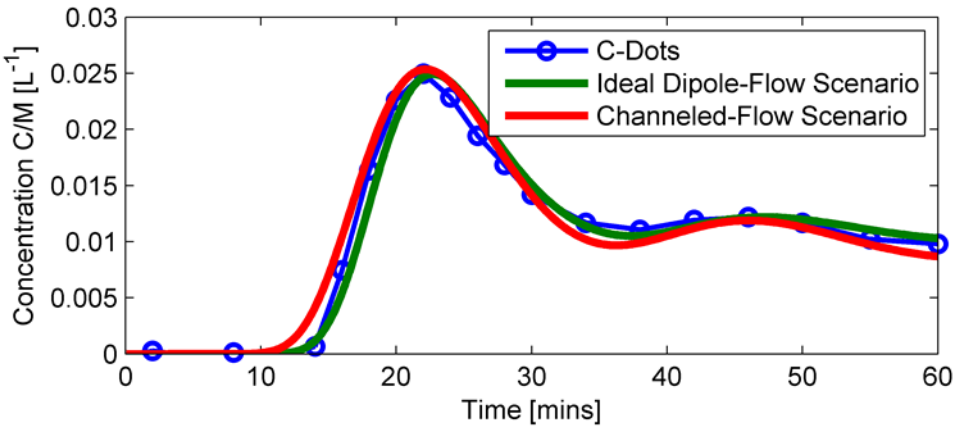

Figure 10: Comparison of the experimentally observed C-Dot RTD with the two model scenarios. The fracture aperture spatial distributions used in the tracer simulation curves are shown in Figure 9. Note that the tracer RTD produced by both aperture distributions are nearly identical to the observed conservative tracer RTD.

Once a sufficient fit between the two conservative tracer simulations and the experimentally observed conservative tracer RTD was achieved (see Figure 10), the same aperture distribution shown in Figure 9 was used to simulate thermal breakthrough. These simulations were then compared to experimentally observed thermal breakthrough. Good agreement was found between the observed thermal breakthrough and the model prediction for the channeled-flow scenario (see Figure 11). In contrast, the ideal dipole-flow scenario produces no temperature rise for the entire duration of the experiment despite its nearly identical

conservative tracer RTD simulations shown in Figure 10. In map view, the spatial distribution of temperature rise resulting from the heat exchange simulations reveal the ideal dipole-flow scenario produced a relatively even, radial pattern emanating from injection well 204 (Figure 12). In contrast, the channeled-flow scenario produced a temperature rise that was spatially distributed directly between the injection well and production well consistent with the preferential flow channel created by the large fracture aperture region directly connecting the two wells.

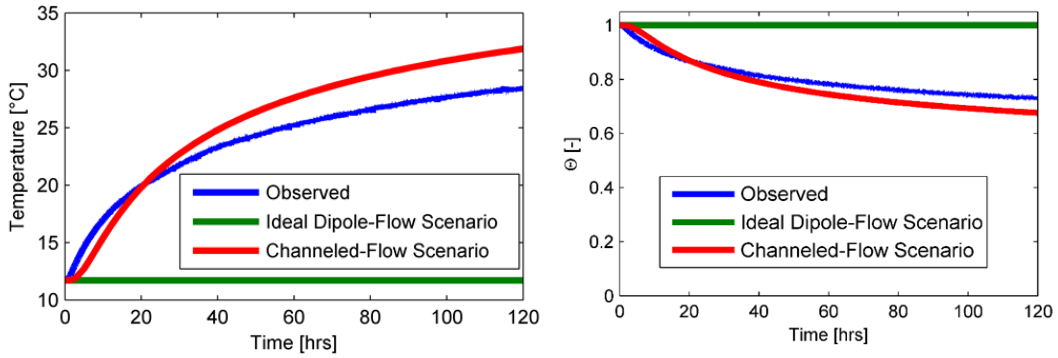

Figure 11: Comparison of simulated and experimentally observed thermal breakthrough. Raw temperature is shown on the figure to the left and normalized temperature is shown on the right. Temperature is normalized such that "1" corresponds to the initial produced groundwater temperature and "0" is the injected temperature. Normalized temperature is calculated by $\Theta = (T(t)-T_w)/(T_r-T_w)$, where $T(t)$, T_w, and T_r, are production temperature as a function of time, temperature of the injection water, and initial groundwater temperature, respectively. The "ideal dipole-flow scenario" produces no temperature rise over the length of the experiment. In contrast, the "channeled-flow scenario" produces early and rapid thermal breakthrough, consistent with experimentally observed data. The difference in fits is dramatic, considering the observed conservative tracer RTD and both model scenario simulations match well (see Figure 10).

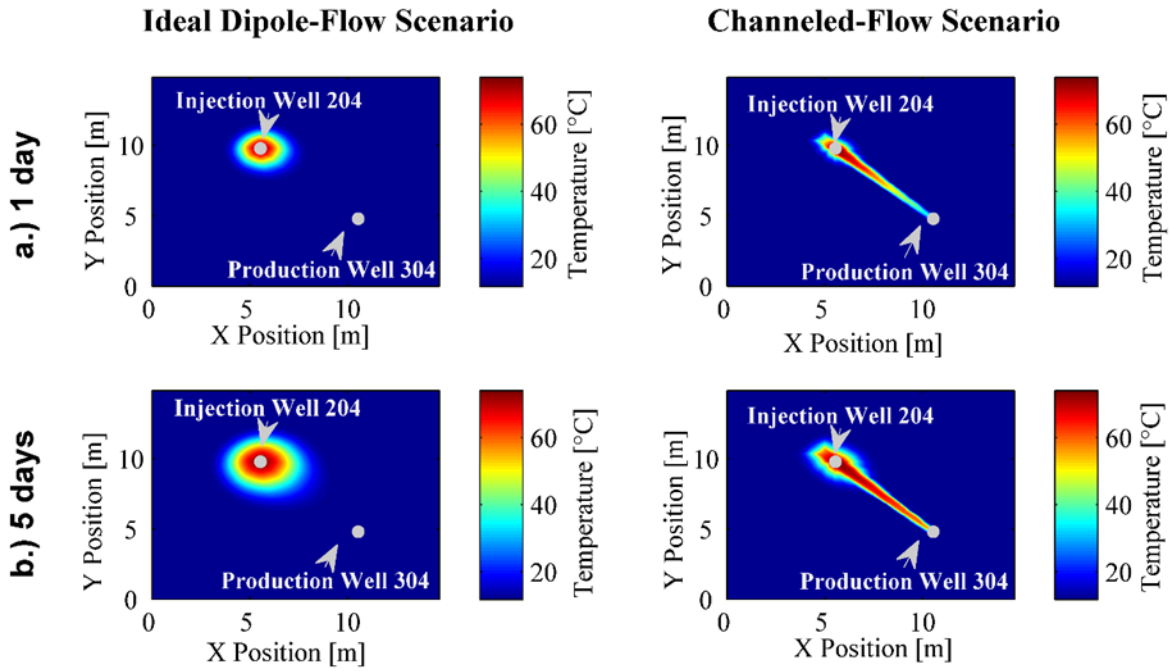

Figure 12: Map view of simulated spatial temperature distributions using the discrete fracture FEM for the "ideal dipole-flow scenario" (left) with a constant aperture and the "channeled-flow scenario" (right) with inlet/outlet well short-circuiting. The top row (Figure 12 a) shows predicted behavior after 1 day of hot water injection for both scenarios and the bottom row (Figure 12 b) shows predicted behavior after 5 days. The ideal dipole-flow scenario results in a temperature distribution that is spread radially from the injection well whereas the channeled-flow

scenario results in a temperature distribution that is preferentially focused in a narrow path directly between the injection well and production well.

The next modeling step involved the use of the thermally reactive tracer data. In order to adequately model thermally reactive tracer behavior, the pre-exponential factor, A, and the activation energy, E_a, of the phenyl acetate hydrolysis reaction (Equation 1) must be known. Attempts were made to measure these parameters in the laboratory. However, there is a discrepancy between the reaction rates measured in the lab and the reaction rate observed in the field prior to hot water injection (i.e. when the groundwater was uniformly 11.7 °C). In laboratory experiments, the pre-exponential factor and activation energy were found to be $1.9785 \cdot 10^8$ hr^{-1} and 56.20 kJ/mol, respectively. These experiments were conducted using Altona groundwater collected roughly 6 months prior. Immediately before the laboratory experiments, the ground water was filtered through a 0.2 µm filter and the pH was measured to be 6.0. These Arrhenius parameters result in a half-life of 70.82 hrs at 11.7°C. The half-life observed in the field, however, was dramatically lower at 0.92 hrs. Since higher pH results in a lower half-life (Nottebohm et al., 2012), it is possible that the discrepancy is related to a difference in pH, since pH of the ground water measured in the field was 6.52. Active research is underway to measure the influence of pH, as well as salinity and buffers, on the kinetics of phenyl acetate hydrolysis.

In this study, the Arrhenius parameters were determined by fitting the channeled-flow scenario's thermally reactive tracer simulation to the observed thermally reactive tracer RTD by manually varying the pre-exponential factor and the activation energy. While this approach does not confirm that the channeled-flow scenario is a more accurate representation of the flow pattern that existed in the field experiments, it does help to illustrate that the thermally reactive tracer curves are capable of distinguishing between two flow patterns better than the conservative tracer tests. The thermally reactive tracer simulations were performed using the fracture aperture distribution and temperature distribution shown in Figure 9 and Figure 12, respectively. The Arrhenius parameters were inferred by varying the pre-exponential factor and activation energy until a reasonable fit between the experimentally observed phenyl acetate RTDs and the channeled-flow scenario's RTDs was achieved. A pre-exponential factor and activation energy of $1.9674 \cdot 10^9$ hr^{-1} and 58.4 kJ mol^{-1}, respectively, were found to provide a sufficient fit to experimentally observed data. These same Arrhenius parameters were then used in the ideal dipole-flow scenario to demonstrate the difference in thermally reactive tracer concentration expected given two different fracture aperture distributions and the temperature field produced after 1 day of heating. As shown in Figure 13, the differences in temperature distribution between the two end-member scenarios produce two tracer RTDs that are significantly different in terms of the thermally reactive tracer concentration profile even though the conservative tracer simulations from the two scenarios match the experimentally observed C-Dot tracer RTD as shown in Figure 10.

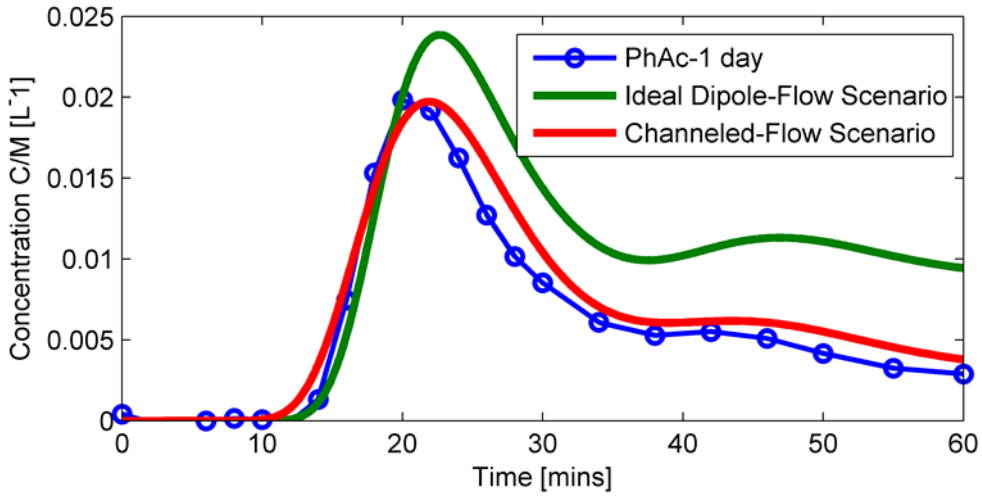

Figure 13: Comparison of the experimentally observed phenyl acetate tracer RTD with the thermally reactive tracer simulations after 1 day of hot water injection for both the "ideal dipole-flow scenario" with a constant aperture and the "channeled-flow scenario" with inlet/outlet well short-circuiting. Using fitted Arrhenius parameters ($A=1.9674 \cdot 10^9$ hr^{-1} and $E_a=58.4$ kJ/mol), simulations were carried out using the temperature distributions of Figure 12 and the aperture distributions of Figure 9. Please note that the Arrhenius parameters were varied using the "channeled-flow scenario" (see Figure 12 a) until they adequately fit the observed thermally reactive tracer curve. These same fitted-parameters were then used for predictions from the "ideal dipole-flow scenario" (Figure 12 a). While fitting parameters to the channeled flow scenario is consistent with the measured thermally reactive tracer RTD, it is not a confirmation of the reservoir structure, but does illustrate the anticipated differences in thermally reactive tracer concentration as a function of time.

5. DISCUSSION

In conjunction with reservoir modeling, the thermally reactive/conservative tracer data was used to identify possible ground water flow patterns that existed between the injection and production well at Altona. Two different scenarios were considered which represent two end-members of possible fracture aperture distributions. The first scenario consisted of a constant fracture aperture which produces an ideal dipole-flow pattern between the injection and production well (referred to as the "ideal dipole-flow scenario"). The second scenario considered an extreme flow channeling case in which a very narrow (1 m) flow channel existed directly in-between the injection and production well (referred to as the "channeled-flow scenario"). While neither of these aperture distributions represent the true aperture field at Altona, they do help identify which flow scenario is more realistic.

Both the channeled-flow scenario and the ideal dipole-flow scenario were equally effective in matching conservative tracer simulations to experimentally observed C-Dot tracer RTD. To adequately fit the experimentally observed tracer RTD, the mean aperture of the channeled-flow scenario had to be significantly larger than in the ideal dipole-flow scenario. The channeled-flow scenario utilized a high aperture region directly between the injection well and production well with a width of 1 m.

The results of the thermally reactive tracer tests reveal that the extent of phenyl acetate reaction increased with the advancement of the induced thermal front. This shows that the reaction kinetics of phenyl acetate hydrolysis were sufficiently dependent upon temperature even in the extremely small temporal and spatial scale encountered at the Altona field site. Interpretation of the thermally reactive tracer data is currently limited because of a discrepancy between laboratory measured reaction rates and reaction rates observed in the field. For now, the Arrhenius parameters were determined based on fitting the thermally reactive tracer simulation results in the channeled-flow scenario to observed data. When these Arrhenius parameters were used in the ideal dipole-flow scenario, the simulated thermally reactive tracer curve was substantially greater in concentration than the tracer curve associated with the channeled-flow scenario. Despite bias towards the channeled-flow scenario, the significance of using a thermally reactive tracer is nevertheless illustrated by the fact that the two fracture aperture scenarios produce significantly different thermally reactive tracer RTDs (see Figure 13). This suggests that the spatial distribution of fluid flow in the subsurface is better constrained when using a thermally reactive tracer than by the use of a conservative tracer alone.

The ideal dipole-flow scenario and the channeled-flow scenario produce dramatically different thermal breakthrough simulations. Only the channeled-flow scenario produces thermal breakthrough consistent with the experimentally observed temperature data. In fact, the ideal dipole-flow scenario produces no temperature rise over the timespan considered whereas both the observed data and the channeled-flow scenario encounter temperature rise of roughly 19 °C or 30% of the difference between injection temperature and the initial ambient groundwater temperature. The poor agreement between experimentally observed vs. predicted thermal breakthrough from the ideal dipole-flow scenario might be considered surprising given the close agreement with the conservative tracer simulations which all show a similar RTD. However, the conservative tracer tests are similar because they both have similar reservoir fluid volumes. The heat transfer surface area, however, is substantially different between the two scenarios and thus produces much different thermal breakthrough.

Temperature measurements recorded via FODTS during the heat exchange experiment corroborates our proposed interpretation described above that a narrow, direct flow channel is present between the injection and production well. Compare for instance the relative magnitude of heat exchange between borehole b5 (located near the production well), and boreholes b9 and b4 (both located half-way between the injection and production well and 2.5 m from the direct path between the two wells) in Figure 6. Despite being several meters further from the injection well, b5 experienced greater heat exchange than both b9 and b4. Based on the location and magnitude of temperature measurements recorded via FODTS we are able to constrain the width of the flow channel to less than 5 m (i.e. the distance between b4 and b9). Consistent with this interpretation is observations of high heat exchange also occurring in boreholes b8 and b6, which are both in the direct path between the injection and production well (see Figure 6). Locations increasingly far from the direct path between the injection and production well generally experienced increasingly less heat exchange. Borehole b10 is an exception as it experienced high heat exchange.

A qualitative evaluation of GPR imaging of saline fluid flow through the fracture further corroborates our proposed interpretation. Saline tracer is confined to a relatively direct path between injection well 304 and production well 204. The region closest to well 104 recorded nearly no change in groundwater salinity which is consistent with the heat exchange recorded in boreholes b1, b2, and b3. The region closest to well 504 recorded a modest change in salinity which is also consistent with the distribution of heat exchange, as indicated by the modest temperature rise observed in boreholes b10, b9, and b7. The greatest change in radar wave phase occurred within a very narrow channel of roughly 1 m directly between well 304 and 204. The high heat exchange observed at b10 and low heat exchange at b1 is consistent with the GPR imaging of salinity in the area as the region around b10 experienced a greater electromagnetic wave phase change compared to the region around borehole b1.

6. CONCLUSIONS

The field experiments conducted in the Altona field site have shown that thermally reactive chemical tracers provide a means to map the progression of the thermal front in a fractured reservoir undergoing heat exchange with circulating fluids. Thermal-chemical-hydraulic modeling results for the system was consistent with field data providing greater insight into the distribution of fracture apertures within the reservoir. To the best of our knowledge, this is the first field experiment that successfully demonstrated that thermally reactive tracers can monitor transient subsurface temperature changes during heat exchange. The

results illustrate how a thermally reactive tracer can be used to better characterize the flow distribution between an injection and production well and, consequentially, provide more accurate forward-models of production well temperature.

Computational models of conservative tracer transport in a discrete fracture indicate there is no unique aperture distribution that fits the conservative tracer RTD (see Figure 10). Both an ideal dipole-flow scenario and a channeled-flow scenario could produce good agreement between simulated and experimentally observed conservative tracer RTD, because both produced similar average reservoir fluid volumes. These same two end-member scenarios, however, produce dramatically different thermal breakthrough curves, because the heat transfer surface area differed. Only the channeled-flow scenario produced thermal breakthrough consistent with the early and rapid temperature rise recorded in the production well during field experimentation. This suggests that the flow distribution between the two wells resembled the channeled-flow scenario more than the ideal dipole-flow scenario.

Experimental evidence that corroborates the interpretation that a narrow flow channel exists includes the spatial distribution of temperature recorded via FODTS (Figure 6) and GPR imaging of salt transport within the fractured reservoir (Figure 4). GPR imaging of the spatial distribution of flow paths between the injection and production well showed that a narrow (roughly 1 to 5 m) channel existed over the 14 m distance between the injection and production well. The spatial distribution of heat exchange recorded via FODTS was consistent with the distribution of tracer imaged via GPR.

The results of these experiments highlight the importance of considering fracture aperture distribution, not just the mean fracture aperture, even in a single fracture. In the Altona reservoir, while the mean fracture aperture was a major controlling factor of the conservative tracer RTD, it had no effect on the onset and rate of thermal breakthrough. The aperture distribution, however, does matter. For example, flow channeling between injection and production wells can lead to low fluid sweep efficiency in the fracture by reducing the effective surface area available for heat exchange. It appears, at least for the system at Altona, that significant reservoir fluid volumes can still persist in channeled flow. Because conservative tracers RTDs are not influenced by the fluid/rock surface area, they only provide measurements of mean and modal reservoir fluid volumes.

Inclusion of a thermally reactive tracer in a series of tracer tests conducted during energy production provides a means to monitor and predict transient subsurface temperature. This study demonstrated this capability at the Altona site in a well characterized meso-scale fracture system. This first field validation is very encouraging, suggesting that properly designed thermally reactive tracers can be used to determine heat extraction performance in larger, commercial-sized geothermal reservoirs. When used with inert tracer and other geophysical information thermally reactive tracers have potential to improve reservoir management strategies to maximize system performance.

7. FUTURE PLANS

Future laboratory work will attempt to replicate the phenyl acetate reaction rate constant observed in the field such that known, rather than inferred, Arrhenius parameters may be applied to computational modeling of thermally reactive tracer transport. Future attempts to infer the spatial distribution of fracture aperture at the Altona field site using these reactive and conservative tracer data will make use of the fact that spatial aperture variations have been shown to have a self-affine spatial correlation governed by a roughness or “Hurst” coefficient (Fox, Koch, and Tester, 2015). We will determine the optimum fracture aperture field based on fitting a simulated tracer RTD to experimentally observed field data using an inverse search methodology based on principal component analysis and a genetic algorithm. This aperture field will then be used to produce forward-models of thermal breakthrough and the result will be compared to the experimentally observed thermal breakthrough presented in this paper.

8. ACKNOWLEDGEMENTS

This study was funded through partial support from the Department of Energy’s Geothermal Technologies Program (DE-EE0006764 and DE-EE0002767), the National Science Foundation’s Earth Energy IGERT program, and the Cornell Energy Institute. The authors thank the William H. Miner Agricultural Research Institute for providing access to their facilities, including their Environmental Laboratory and the Altona Flat Rock site. Special thanks to Steve Kramer, Director of Lab Studies at the Miner Institute, for providing laboratory technical support for this study. The authors would also like to thank Ivan Beentjes, Sean Hillson, Koenraad Beckers, and Maciej Lukawski for providing much appreciated assistance during field experiments and Elizabeth Bach for assisting in the preparation of groundwater samples for laboratory analysis.

REFERENCES

Becker, M. W., Remmen, K., Tsoflias, G., Reimus, P., and Hawkins, A. J.: Investigating well connectivity and reactive surface area in a sandstone bedrock using ionic tracers, presentation at NGWA Conference on Groundwater in Fractured Rock and Sediments, Burlington, Vermont (2013).

Becker, M. W., and Tsoflias, G. P.: Comparing flux-averaged and resident concentration in a fractured bedrock using ground penetrating radar, *Water Resources Research,* **46**, doi:W09518 (2010).

Castagna, M., Becker, M. W., and Bellin, A.: Joint estimation of transmissivity and storativity in a bedrock fracture, *Water Resources Research,* **47**. doi:10.1029/2010wr009262, (2011).

Fox, D. B., Koch, D. L., and Tester, J. W.: The effect of spatial aperture variations on the thermal performance of discretely fractured geothermal reservoirs, *Geothermal Energy,* **3**, doi:10.1186/s40517-015-0039-z, (2015), 1-29.

Guiltinan, E. J., and Becker, M.: Using Harmonic hydraulic tests to estimate fracture bedrock properties and predict local heterogeneity, *Presentation,* Geological Society of America (2010).

Hawkins, A. J., and Becker, M. W.: Measurement of the spatial distribution of heat exchange in a geothermal analog bedrock site using fiber optic distributed temperature sensing*, Proceedings,* 37th Workshop on Geothermal Reservoir Engineering, Stanford, California (2012).

Hawkins, A. J., Fox, D. B., Zhao, R., Tester, J. W., Cathles, L. M., Koch, D. L., and Becker, M. W.: Predicting Thermal Breakthrough from Tracer Tests: Simulations and Observations in a Low-Temperature Field Laboratory, *Proceedings,* 47th Workshop on Geothermal Reservoir Engineering, Stanford, California (2015).

Krysmann, M. J., Kelarakis, A., Dallas, P., and Giannelis, E. P.: Formation Mechanism of Carbogenic Nanoparticles with Dual Photoluminescence Emission, *Journal of the American Chemical Society,* **134**, doi:10.1021/ja204661r, (2012), 747-750.

Li, Y. V., Cathles, L. M., and Archer, L. A.: Nanoparticle tracers in calcium carbonate porous media, *Journal of Nanoparticle Research,* **16**, doi:10.1007/s11051-014-2541-9, (2014).

Maier, F., Schaffer, M., and Licha, T.: Temperature determination using thermo-sensitive tracers: Experimental validation in an isothermal column heat exchanger, *Geothermics,* **53**, doi:10.1016/j.geothermics.2014.09.007, 533-539, (2015).

Nottebohm, M., Licha, T., and Sauter, M.: Tracer design for tracking thermal fronts in geothermal reservoirs, *Geothermics,* **43**, doi:10.1016/j.geothermics.2012.02.002, (2012), 37-44.

Olcott, P., G.: *Ground Water Atlas of the United States*. Reston, Virgina, (1995).

Ray, S. C., Saha, A., Jana, N. R., and Sarkar, R.: Fluorescent Carbon Nanoparticles: Synthesis, Characterization, and Bioimaging Application, *Journal of Physical Chemistry C,* **113**, 18546-18551. doi:10.1021/jp905912n, (2009).

Rayburn, J. A., Knuepfer, P. L. K., and Franzi, D. A.: A series of large, Late Wisconsinan meltwater floods through the Champlain and Hudson Valleys, New York State, USA, *Quaternary Science Reviews,* **24**, (2005), 2410-2419.

Robertson, E. C.: Thermal properties of rocks, retrieved from http://pubs.er.usgs.gov/publication/ofr88441, (1988), 88-441.

Robinson, B. A., Tester, J. W., and Brown, L. F.: Reservoir Sizing Using Inert and Chemically Reacting Tracers, *SPE Formation Evaluation,* **2**, (1988).

Sensornet.: ORYX DTS user manual, (2007).

Smolen, J., and Spek, S.: A DTS primer for oil and gas production: SHELL oil and gas, (2003).

Talley, J.: Imaging channelized flow in fractured rock using surface GPR, *Masters Thesis*, University of Buffalo, Buffalo, (2005).

Talley, J., Baker, G. S., Becker, M. W., and Beyrle, N.: Four dimensional mapping of tracer channelization in subhorizontal bedrock fractures using surface ground penetrating radar, *Geophysical Research Letters,* **32**, (2005).

Tsang, C. F., and Neretnieks, I: Flow channeling in heterogeneous fractured rocks, *Reviews of Geophysics,* **36**, doi:10.1029/97rg03319, (1998), 275-298.

Tsoflias, G. P., Baker, M., and Becker, M. W.: Field GPR monitoring of flow channeling in fractured rock, *Presentation,* American Geophysical Union Fall Meeting, San Francisco, CA, (2012).

Tsoflias, G. P., and Becker, M. W.: Ground-penetrating-radar response to fracture-fluid salinity: Why lower frequencies are favorable for resolving salinity changes, *Geophysics,* **73**, J25-J30. doi:10.1190/1.2957893, (2008).

Tsoflias, G. P., Perll, C., Baker, M., and Becker, M. W.: Cross-Polarized GPR Imaging of Fracture Flow Channeling, *Journal of Earth Science,* **26,** doi:10.1007/s12583-015-0612-1, (2015), 776-784.

Van de Giesen, N., Steele-Dunne, S. C., Jansen, J., Hoes, O., Hausner, M. B., Tyler, S., and Selker, J.: Double-Ended Calibration of Fiber-Optic Raman Spectra Distributed Temperature Sensing Data, *Sensors,* **12,** doi:10.3390/s120505471, (2012), 5471-5485.